Contributions of Moist Convection and Internal Gravity Waves to Building the Atmospheric −5/3 Kinetic Energy Spectra

Y. QIANG SUN

Department of Meteorology, and Center for Advanced Data Assimilation and Predictability Techniques, The Pennsylvania State University, University Park, Pennsylvania, and National Center for Atmospheric Research, Boulder, Colorado

RICHARD ROTUNNO

National Center for Atmospheric Research, Boulder, Colorado

FUQING ZHANG

Department of Meteorology, and Center for Advanced Data Assimilation and Predictability Techniques, The Pennsylvania State University, University Park, Pennsylvania

(Manuscript received 27 March 2016, in final form 3 October 2016)

ABSTRACT

With high-resolution mesoscale model simulations, the authors have confirmed a recent study demonstrating that convective systems, triggered in a horizontally homogeneous environment, are able to generate a background mesoscale kinetic energy spectrum with a slope close to −5/3, which is the observed value for the kinetic energy spectrum at mesoscales. This shallow slope can be identified at almost all height levels from the lower troposphere to the lower stratosphere in the simulations, implying a strong connection between different vertical levels. The present study also computes the spectral kinetic energy budget for these simulations to further analyze the processes associated with the creation of the spectrum. The buoyancy production generated by moist convection, while mainly injecting energy in the upper troposphere at small scales, could also contribute at larger scales, possibly as a result of the organization of convective cells into mesoscale convective systems. This latter injected energy is then transported by energy fluxes (due to gravity waves and/or convection) both upward and downward. Nonlinear interactions, associated with the velocity advection term, finally help build the approximate −5/3 slope through upscale and/or downscale propagation at all levels.

1. Introduction

The energy spectrum of the atmosphere and its underlying physical mechanisms remain active research topics despite decades of observations and scientific research. Long-range passenger aircraft have collected velocity and temperature measurements since the 1970s. These measurements indicate an energy spectrum varying as k^{-3} (k is wavenumber) or a −3 energy spectrum at synoptic scales with a transition to a −5/3 spectrum within the mesoscale (<500 km) (Nastrom and Gage 1985). Charney's theory of geostrophic turbulence (Charney 1971) is the generally accepted explanation of the synoptic-scale −3 spectrum. However, there is no general agreement on the mechanism(s) behind the mesoscale −5/3 spectrum. Many hypotheses for explaining the spectrum at the mesoscale have been proposed, including, but not limited to, an inverse two-dimensional (2D) cascade of small-scale energy produced perhaps by convection (Lilly 1983), production of inertia–gravity waves (e.g., VanZandt 1982; Koshyk et al. 1999), the signature of stratified turbulence at scales where rotational constraints become less important (Lindborg 2006), and the nature of surface quasi geostrophy (SQG) due to the development of fronts at the edge of synoptic-scale cyclones and anticyclones at the top of the troposphere (Tulloch and Smith 2006).

The abovementioned mechanisms for the −3 and −5/3 spectra are based on idealized models. Several

Corresponding author e-mail: Professor Fuqing Zhang, fzhang@psu.edu

DOI: 10.1175/JAS-D-16-0097.1

full-physics models have successfully captured the observed transition of the spectrum slope from −3 to −5/3 (e.g., Skamarock 2004; Hamilton et al. 2008; Skamarock et al. 2014), yet only limited discussion has been given to explain the mechanism(s) behind it. None of these earlier studies looked into the details of the growth process of the mesoscale energy spectrum. Recently, Waite and Snyder (2013) found that moist processes could energize the mesoscale and thus help the transition of the slope. A similar full-physics idealized baroclinic wave simulation in Sun and Zhang (2016) also found this distinct transition of the simulated kinetic energy spectrum at a scale of ~400 km in their moist experiment. Interestingly the dry experiment in their study maintains the steep −3 slope all the way to the mesoscale in the upper troposphere. This result emphasizes the critical role of moist convection in the creation of the shallower −5/3 slope. Compared to the dry experiment, moist convection generates many gravity wave–like signals at the upper levels of the troposphere (Wei and Zhang 2014, 2015; Wei et al. 2016), which might be responsible for the spectrum transition from −3 to −5/3 at those levels. More recently, Durran and Weyn (2016) shows that a −5/3 spectrum evolves and reaches to scales comparable to observations in their simulations of convective cloud systems.

Motivated by these recent findings, this study aims to investigate the mechanisms responsible for the −5/3 slope in Durran and Weyn (2016), especially the contributions of moist convection and internal gravity waves generated by convective systems. This study confirms their finding of an approximate −5/3 spectrum and provides new information for each specific height level. The remainder of the paper is organized as follows: Section 2 introduces the model setup for our simulation. Section 3 gives a brief overview of the simulation and analyzes the evolution of the mesoscale energy spectrum through a spectral energy budget. Further discussion and concluding remarks are given in section 4.

2. Methodology

The Weather Research and Forecast (WRF) Model, version 3.6.1, (Skamarock et al. 2008) is used in an idealized mode for this study. The domain size of the simulation is 800 km × 800 km, with a horizontal grid spacing of 2 km. The model top is fixed at 20 km. To get an accurate calculation of the kinetic energy spectra budget, we have 200 layers in the vertical direction. The vertical grid spacing is approximately 100 m, although the vertical layers are not equally spaced in the WRF Model. The Coriolis force is neglected, unless otherwise stated. Periodic lateral boundary conditions are implemented here to facilitate the spectral analysis. To further simplify both the model and the interpretation, we use a free-slip bottom boundary condition in the simulation. No PBL or surface scheme is used in the current simulation. Also, no cumulus or radiation parameterizations are used. Near the upper boundary, an absorbing layer, as described by Klemp et al. (2008), is applied for the uppermost 5 km of the model domain to reduce artificial reflection of gravity waves. This sponge layer has proved successful in the idealized squall-line simulation done by Klemp et al. (2008). The Morrison scheme is used for the microphysics parameterization (Morrison et al. 2009). The time step for the integration of the model is 3 s.

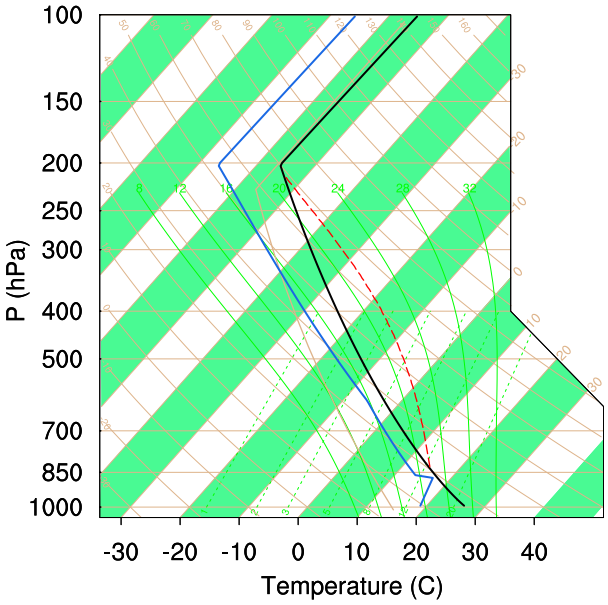

FIG. 1. Skew T diagram of the thermodynamic sounding profile used for all simulations presented herein. The sounding has a CAPE of ~2000 J kg^{-1} and a surface mixing ratio of 14 g kg^{-1}.

Figure 1 shows our initial sounding profile for the simulations. It is based on Weisman and Klemp (1982), except that we fix the mixing ratio below 1 km at 14 g kg^{-1} and cap the RH at 75% for any level above 1.4 km. A unidirectional horizontally uniform background wind profile is specified in which the zonal winds linearly increase from −10 m s^{-1} at the surface to 10 m s^{-1} at a height of 5 km and remain 10 m s^{-1} at higher levels (Fig. 2a).

Seven localized warm bubbles with a positive temperature anomaly of 3 K are put into the initial condition to initiate convection. These warm bubbles are aligned from north to south at the domain center, with a

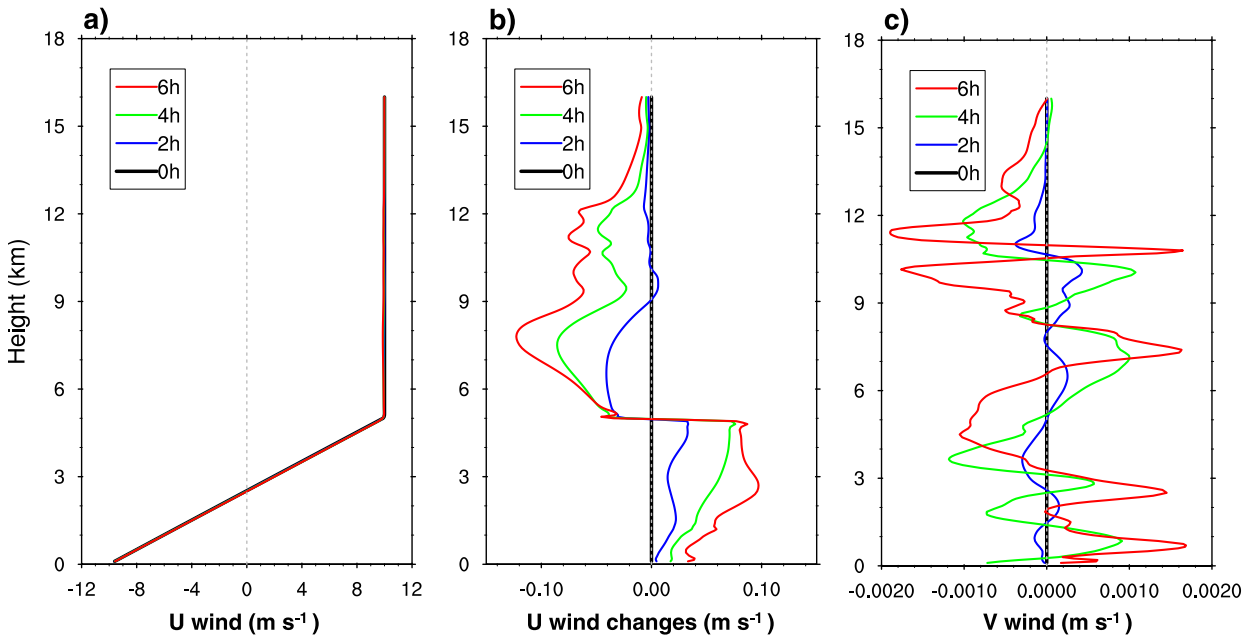

FIG. 2. Vertical profiles of (a) zonal-mean wind and the changes from the initial mean averaged over each horizontal plane and all 20 ensemble members for (b) zonal and (c) meridional winds.

horizontal radius of 10 km and a vertical radius of 1.5 km. Their centers lie at 1.5 km above the surface, with a horizontal distance of 20 km away from each other. The warm bubbles, each evolving into a convective cell, then interact with each other under the wind shear. The evolution of these cells will be briefly introduced in the next section. A 20-member ensemble is produced through perturbing the water vapor mixing ratio in the lowest 1 km with a Gaussian white noise of 0.5 g kg^{-1} to reduce case dependency in the statistics. All the simulations are integrated for 6 h, with fields output every 30 s. The output fields are interpolated to constant height levels with a vertical interval of 50 m to facilitate the calculation of the spectra.

3. Results

a. *Overview of the simulation*

Before we start the spectral analysis, we would like to first take a look at the evolution of our simulation. Figure 3 visualizes the development of the convective cells in one member of our ensemble. Initially (0–2 h), each warm bubble evolves into a convective cell of similar scale, with a strong embedded updraft. After 2 h, the convective cells start to interact with each other under the vertical wind shear. While the convective cells in the middle of the line get weaker, the cells at both ends of the line become stronger and "eat" all the other cells gradually. At the end of the 6-h simulation, two supercell-like systems form at both ends of the line. Slightly different from our expectations, these cells do not organize into a squall line in almost all the ensemble members. This is likely because of the relatively deep vertical wind shear in our simulation. Another possible reason is that the initial line of warm bubbles is perpendicular to the wind shear direction. Sensitivity runs of adding the warm bubbles at different zonal locations and/or adding vertical shear in the meridional direction are more favorable for the formation of a squall line. As a result of this weak organization of the convective cells, the cold pools are also relatively weak in our simulation. The gray shading in Fig. 3 depicts the anomaly virtual potential temperature less than −0.5°C. Compared to Skamarock et al. (1994), both the range and absolute value of the cold-pool temperatures are smaller, which implies a weaker convective system in our simulation. Despite these differences between our simulated convective system and previous studies, their effects on the spectrum are not critical, as we will show later in further sensitivity experiments.

Strong gravity waves can be generated by these convection cells. Figure 4a shows a south–north cross section over the domain center at 2 h for the same ensemble member as shown in Fig. 3. The location of each convective cell can be identified by the 25-dBZ reflectivity line. The region with vertical velocity greater than 0.1 m s^{-1} is shaded in cyan, while the potential temperature is plotted using gray lines. Clear gravity wave

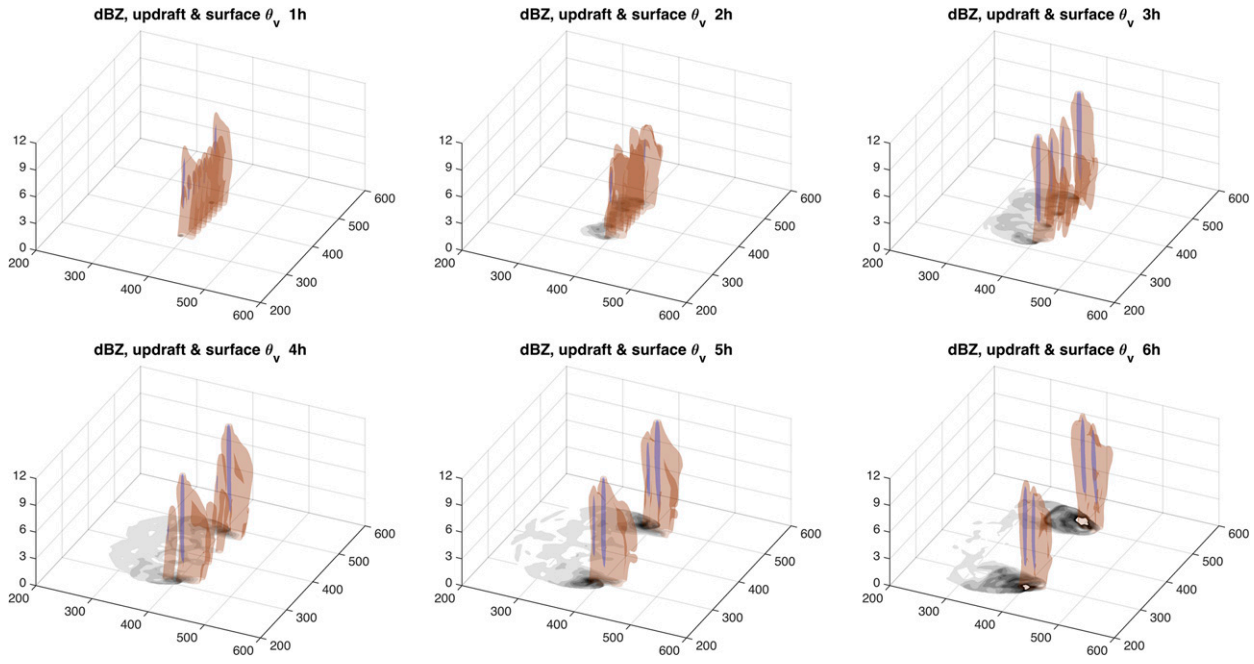

FIG. 3. Time evolution of simulated convective cells in one of the ensemble members. The isosurface of vertical velocity (w = 10 m s^{-1}; purple), radar reflectivity (25 dBZ; brown), and surface cold pool contours (θ_v anomaly < -0.5°C; gray) are plotted every hour.

signals generated by the convective cells can be found at levels above 12 km (lower stratosphere), where the vertical velocity and the potential temperature show a quadrature phase relationship. In the troposphere, as a result of turbulent motions induced by the convection cells, linear gravity wave signals cannot be easily identified. This result is further supported by the profile of the domain-averaged vertical heat transport ($\overline{w'T'}$; Fig. 4b). Since linear nongrowing gravity waves that have a quadrature relationship between w and T do not transfer heat, we see negligible transport at levels above 12 km; whereas for the troposphere, there is considerable heat

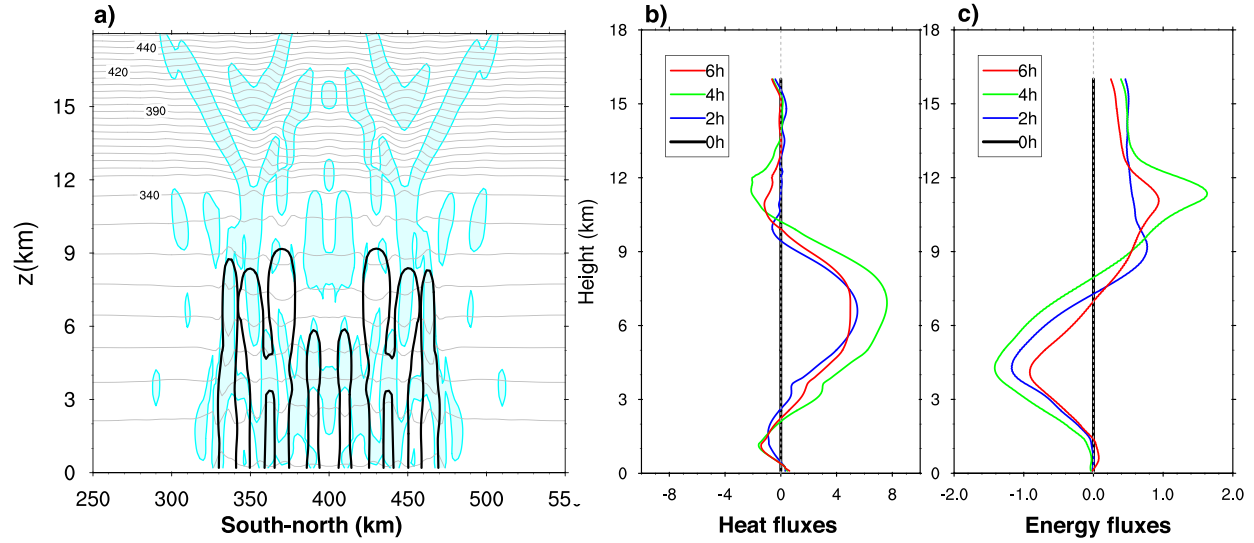

FIG. 4. (a) South–north cross section at the domain center for the same member as in Fig. 3, showing the gravity wave signals and convective activity [$w > 0.1$ m s^{-1} (cyan shaded); dB$Z > 25$ (black line); and potential temperature (gray lines)]. The vertical profiles of (b) heat fluxes ($\overline{w'T'}$; m K s^{-1}) and (c) energy fluxes ($\overline{w'p'}$; m hPa s^{-1}) averaged over all 20 members and displayed every 2 h.

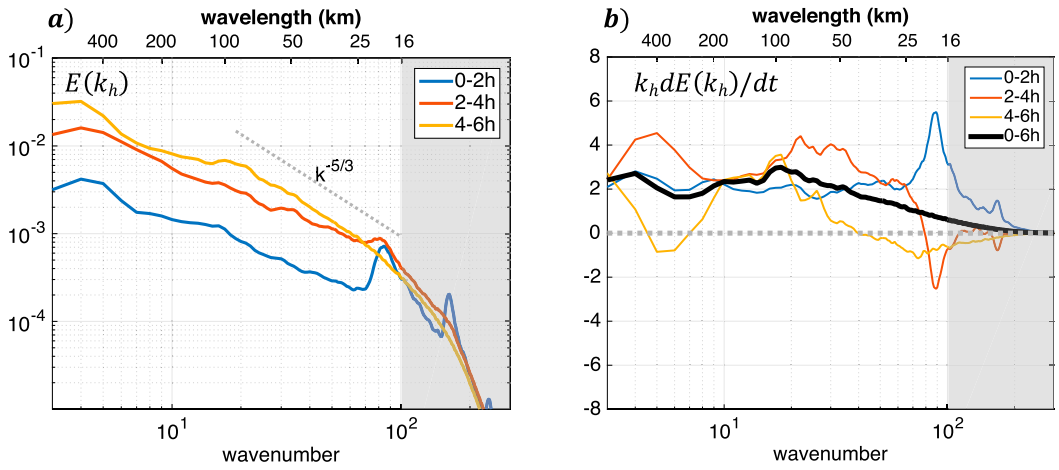

FIG. 5. (a) Time evolution of the kinetic energy spectra ($m^2\,s^{-2}\,kg\,m^{-3}$), averaged between 0 and 15 km over every 2-h period for all the 20 ensemble members. (b) The $k_h^* dE(k_h)/dt$ term ($10^{-6}\,m^2\,s^{-3}\,kg\,m^{-3}$) derived from (a). The tendency terms in (b) are multiplied by horizontal wavenumber k_h in order to preserve the area in a log-linear plot; the black line shows the time average over 0–6 h.

transfer due to convection. Figure 4c also shows the domain-averaged vertical energy flux ($\overline{w'p'}$). According to linear gravity wave theory, upward (downward) propagation of the gravity waves implies positive (negative) vertical energy transport. We will discuss in more detail the energy transport in the spectrum-analysis part of this study.

The convective cells and the gravity waves they generate have a downgradient effect on the mean flow (Fig. 2b). We see a slight increase of the mean zonal wind ($\sim 0.1\,m\,s^{-1}$) in the 0–5-km layer; above 5 km, the mean zonal wind decreases a small amount ($\sim 0.1\,m\,s^{-1}$). This downgradient effect leads to the loss of mean kinetic energy, which will be discussed later. The mean meridional wind is also plotted in Fig. 2c. With the symmetric model setting we used, the mean meridional wind should be zero. Our calculation shows a noisy mean v wind signal with an amplitude of $0.001\,m\,s^{-1}$ (two orders of magnitude smaller than mean zonal wind change) due to numerical error. The accuracy of our calculation demonstrates that the change of the mean zonal wind ($\sim 0.1\,m\,s^{-1}$), thus the loss of the mean kinetic energy, is due to mixing induced by convection and gravity waves.

b. Kinetic energy spectra

The spectrum of the kinetic energy is calculated using the 2D discrete cosine transform (DCT) method (Denis et al. 2002; Peng et al. 2014) at each vertical level. More details on this method can be found in the appendix A. For a 2D field with periodic boundary conditions, the DCT gives results that are very close to those obtained using the discrete Fourier transform, and it is more generally applicable to nonperiodic domains. We use a curly bracket here to denote the DCT spectral coefficients of a field q as $\{q(\mathbf{k})\}$, where $\mathbf{k} \equiv (k_x, k_y)$ is the horizontal wave vector. The dependence of spectral quantities on height z and time t is suppressed for clarity.

By neglecting the density perturbation, we can approximate the total horizontal kinetic energy per unit volume for each specific height level as follows:

$$E_h = \frac{1}{2}\overline{\rho}\iint (\mathbf{u}\cdot\mathbf{u})\,dx\,dy = \frac{1}{2}\overline{\rho}\iint (u^2+v^2)\,dx\,dy, \tag{1}$$

where $\mathbf{u}$ is the horizontal wind vector, and $\overline{\rho}$ is the horizontal averaged density (function of height only). The kinetic energy spectrum $E(k_h)$ can then be defined by

$$\begin{aligned} E_h &= \frac{1}{2}\overline{\rho}\iint (u^2+v^2)\,dx\,dy \\ &= \frac{1}{2}\overline{\rho}\iint [\{u(\mathbf{k})\}\cdot\{u(\mathbf{k})\} + \{v(\mathbf{k})\}\cdot\{v(\mathbf{k})\}]\,dk_x\,dk_y \\ &= \int E(k_h)\,dk_h, \end{aligned} \tag{2}$$

where the horizontal wavenumber k_h is defined as $k_h^2 = k_x^2 + k_y^2$. The kinetic energy spectrum is obtained by taking the sum over wavenumber bands $k_h - \Delta k/2 < k_h \le k_h + \Delta k/2$. Note that these definitions are all based on a 2D plane; thus, we will conduct the calculation at each specified height.

The derived mean kinetic energy spectra, averaged over all 20 ensemble members every 2 h and over all the levels between 0 and 15 km, are shown in Fig. 5. Since the resolution of the simulation is 2 km, signals with a wavelength shorter than 15 km (gray shaded area) are

not well resolved by the model. The slope of the spectrum in this region falls off quickly because of implicit dissipation in the model. Any results within this range should be treated with caution. We will focus here on the well-resolved range (wavelengths > 15 km). For the first 2 h, the energy spectrum clearly shows a peak at a scale around 20 km, which is the scale of the warm bubble and the convective cells. Note that the spectral decomposition of an isolated feature projects onto all scales and most prominently onto the largest scales; thus, the initial large-scale signal in the spectrum analysis is mainly due to the projection of energy associated with the limited extent of the convective cells. After 2 h, the growth of the spectrum extends to larger scales. For the time period between 4 and 6 h, the energy spectrum approaches a quasi −5/3 slope for scales shorter than 100 km. Although there are slightly different evolutions of the convective cells in the 20 members, the evolution of the kinetic energy spectrum is insensitive to the details of the convective cells. All the 20 members have formed the quasi −5/3 slope as in the ensemble-mean result after 6 h of integration. This is consistent with Durran and Weyn (2016), which shows that the kinetic energy spectrum with a slope close to −5/3 could indeed be built solely from convection. Further examinations with a smaller time interval (not shown) indicate that the kinetic energy spectrum at scales smaller than 100 km becomes quasi steady after 5 h, when it reaches the −5/3 slope. We also did one experiment with slightly different model settings in which the simulation was integrated for 8 h. The supercells in that experiment maintain themselves and bring the spectrum at larger scale (>100 km) closer to the −5/3 reference line, though the change is much slower. The growth process of the quasi −5/3 slope for scales less than 100 km in our ensemble experiments is the focus of this study.

The kinetic energy spectrum can also be further decomposed into horizontally rotational and divergent parts, $E_R(k_h)$ and $E_D(k_h)$, which are given by

$$\int E_R(k_h)\,dk_h = \iint \frac{1}{2}\overline{\rho}\frac{\{\zeta\}\cdot\{\zeta\}}{k_h^2}\,dk_x\,dk_y \quad \text{and} \quad (3)$$

$$\int E_D(k_h)\,dk_h = \iint \frac{1}{2}\overline{\rho}\frac{\{\boldsymbol{\sigma}\}\cdot\{\boldsymbol{\sigma}\}}{k_h^2}\,dk_x\,dk_y, \quad (4)$$

where ζ and $\boldsymbol{\sigma}$ are the vertical vorticity and horizontal divergence, respectively. Figure 6 shows the result after the decomposition. Unlike previous studies involving baroclinic waves and moist convection (e.g., Waite and Snyder 2013), the divergent energy spectrum in the present physical situation is not the only component responsible for the shallower −5/3 slope. At the end of the simulation (4–6 h), the rotational kinetic energy also has a quasi −5/3 slope within the wavelength range of 15–100 km. The magnitude of the rotational kinetic energy within the −5/3 slope range (15–100 km) is even slightly larger than that of the divergent kinetic energy. A closer look shows that the ratio of the divergent to the rotational kinetic energy increases with height. In the troposphere, the amplitude of the rotational kinetic energy is stronger because of the mesoscale convective vortices produced by the convective systems (Davis and Weisman 1994). While in the lower stratosphere the divergent kinetic energy dominates over the rotational kinetic energy, as gravity waves are the primary signals there. Analysis of observational datasets in previous studies led to different conclusions with regard to the ratio of divergent to rotational kinetic energy. Callies et al. (2014) conclude that the divergent component of the kinetic energy is slightly stronger for the mesoscale energy spectrum. On the contrary, other studies find that the rotational kinetic energy is more important (Cho et al. 1999; Lindborg 2015). Differences in data analysis and datasets might be responsible for different conclusions (Bierdel et al. 2016). Further study is clearly needed to reach agreement on this.

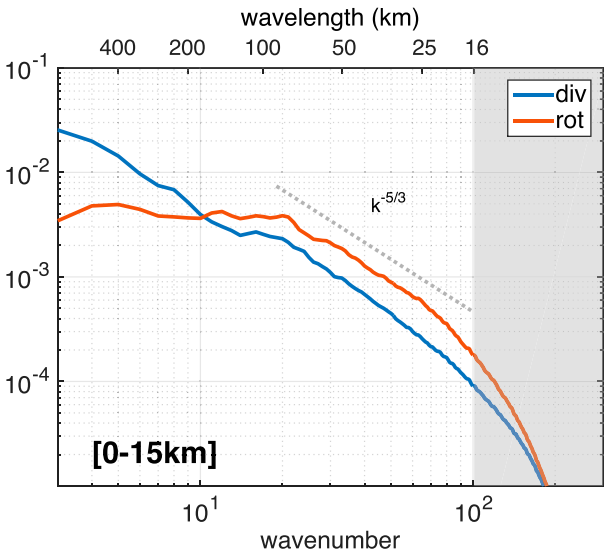

FIG. 6. Ensemble-mean rotational (red) and divergent (blue) kinetic energy spectra ($m^2\,s^{-2}\,kg\,m^{-3}$) averaged between 4 and 6 h. The definitions of rotational and divergent kinetic energy spectra are given in the text.

Figure 7 shows the kinetic energy spectrum averaged over 0–4, 6–10, and 12–15 km (lower troposphere, upper troposphere, and lower stratosphere, respectively). The kinetic energy is stronger in the troposphere than it is in the stratosphere as a result of decreasing density with height. What is more interesting is that, although it

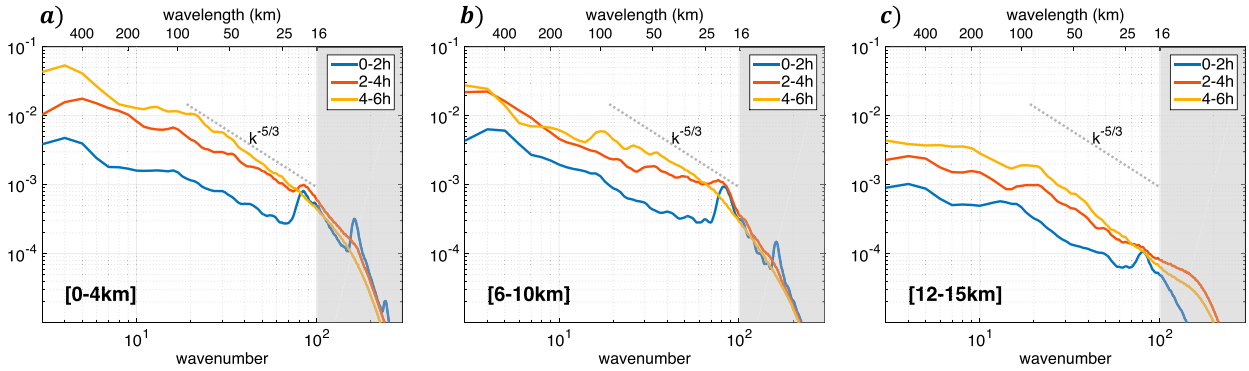

FIG. 7. Kinetic energy spectra ($m^2\,s^{-2}\,kg\,m^{-3}$) as in Fig. 5a, but for averages over different height levels: (a) the lower troposphere (0–4 km), (b) the upper troposphere (6–10 km), and (c) the lower stratosphere (12–15 km).

differs slightly,[1] an approximate −5/3 slope in the wavelength range 15–100 km does show up at all levels throughout the atmosphere toward the end of our simulation (Fig. 7). The upper troposphere, where aircraft measurements lie, is not the only level that has a spectrum slope of −5/3; the lower troposphere and the lower stratosphere also have such a slope. The present model thus offers an alternative to the surface quasigeostrophic hypothesis in Tulloch and Smith (2006). Since no surface scheme or boundary layer scheme is adopted in our simulation, the creation of the kinetic spectrum is clearly due to the convection systems (diabatic heating, which has a maximum in the upper troposphere and a value close to zero near the surface and above the tropopause). Any boundary process plays at most a secondary role since no PBL or surface scheme is used in our simulations.

c. *Spectral budget analysis*

More insight can be gained into the dynamics of the horizontal kinetic energy spectrum by examining processes contributing to the evolution of the spectrum. The tendency of the kinetic energy spectrum is shown in Fig. 5b. The derived tendency term is multiplied by horizontal wavenumber k_h after summed over the wavenumber bands in order to preserve the area in this log-linear plot. Even after this multiplication, for an energy spectrum with a −5/3 power-law slope, it can be proven that the tendency term will decrease with decreasing scale, as is shown by the black line for the range of wavelengths smaller than 100 km. To be clear on the sources and sinks for the energy spectrum $E(\mathbf{k})$, we compute the budget equation for $E(\mathbf{k})$:

$$\frac{\partial E(\mathbf{k})}{\partial t} = A(\mathbf{k}) + P(\mathbf{k}) + D(\mathbf{k}), \tag{5}$$

where the $A(\mathbf{k})$ term is the energy transfer due to advection,

$$A(\mathbf{k}) = -\overline{\rho}\{\mathbf{u}\} \cdot \left\{\mathbf{u} \cdot \nabla_h \mathbf{u} + w\frac{\partial \mathbf{u}}{\partial z}\right\}, \quad \text{and} \tag{6}$$

the $P(\mathbf{k})$ term is the spectral tendency due to the horizontal pressure gradient. If we adopt the Exner function form of the pressure gradient force, $P(\mathbf{k})$ can be written as follows:

$$P(\mathbf{k}) = -\overline{\rho}\{\mathbf{u}\} \cdot \{C_p \theta_v \nabla_h \pi'\}, \tag{7}$$

where C_p is the heat capacity at constant pressure, θ_v is the virtual potential temperature, and π' is the anomaly Exner function. The quantity $D(\mathbf{k})$ in Eq. (5) is simply the dissipation. Note here, all the terms are defined as functions of wave vector $\mathbf{k}$, whereas in the figures, we present each term as a function of the horizontal wavenumber k_h.

As the nonlinear term in the momentum equation, advection is responsible for all the interactions across different scales. The $A(\mathbf{k})$ term in the spectral budget equation acts to redistribute energy between different scales. However, the level-by-level transfer caused by $A(\mathbf{k})$ is not strictly conservative; that is, its sum over all wavenumbers is not zero. In addition to the conservative exchange of kinetic energy between different wavenumbers, $A(\mathbf{k})$ has a contribution from the divergence of vertical kinetic energy flux. To resolve this issue, the $A(\mathbf{k})$ term can be further decomposed as follows:

[1] The calculated linear-fit slope varies from −1.6 to −2.1 for wavelengths between 16 and 100 km at different height levels during 4–6 h of our simulations (linear-fit slope is −1.75 for 0–15 km, −1.90 for 0–4 km, −1.61 for 6–10 km, and −2.05 for 12–15 km). The steeper slope of −2 mainly lies in the stratosphere, especially where the gravity wave signal is relatively weak. For the constant-Coriolis experiment shown in Fig. 12, the slope range is much smaller (from −1.6 to −1.8) as a result of more organized convection (linear-fit slope is −1.69 for 0–15 km, −1.72 for 0–4 km, −1.66 for 6–10 km, and −1.63 for 12–15 km).

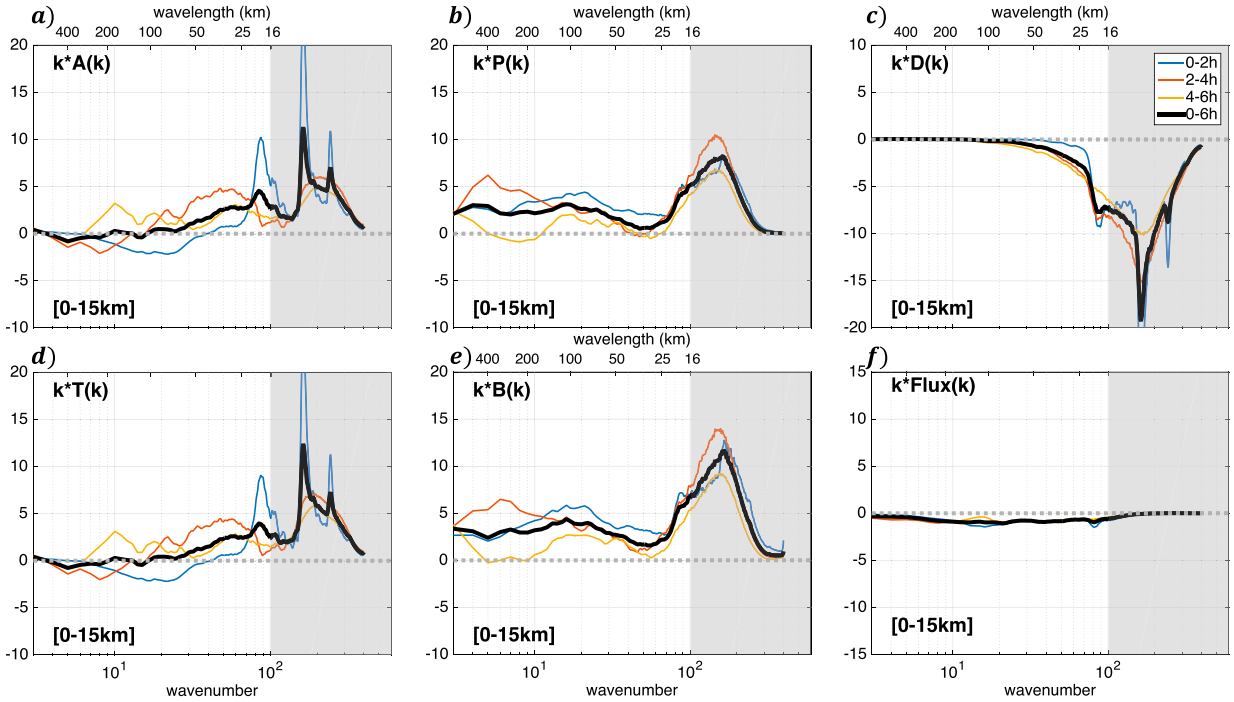

FIG. 8. (a)–(c) Kinetic energy spectrum budget terms ($10^{-6}\,\mathrm{m^2\,s^{-3}\,kg\,m^{-3}}$) in Eq. (5) and (d)–(f) decomposition of advection and pressure terms in Eq. (10) averaged over 0–15 km for all the ensemble members. Refer to the text for details on Eqs. (5) and (10).

$$A(\mathbf{k}) = \underbrace{-\overline{\rho}\{\mathbf{u}\}\cdot\left\{\mathbf{u}\cdot\nabla_h\mathbf{u}+\frac{\mathbf{u}(\nabla_h\cdot\mathbf{u})}{2}\right\}-\frac{1}{2}\overline{\rho}\{\mathbf{u}\}\cdot\left\{w\frac{\partial\mathbf{u}}{\partial z}\right\}+\frac{1}{2}\overline{\rho}\left\{\frac{\partial\mathbf{u}}{\partial z}\right\}\cdot\{w\mathbf{u}\}}_{T(\mathbf{k})}$$
$$\underbrace{-\frac{1}{2}\frac{\partial(\overline{\rho}\{\mathbf{u}\}\cdot\{w\mathbf{u}\})}{\partial z}}_{\text{Divergence of vertical energy flux}}. \tag{8}$$

Proof of this decomposition is given in the appendix B. By separating the vertical energy flux term out, $T(\mathbf{k})$ is the strictly conservative term we need: that is, the sum of $T(\mathbf{k})$ over all wavenumbers is zero [Eq. (B5)].

Similarly, $P(\mathbf{k})$ also includes a contribution due to the divergence of the vertical energy flux. As derived in the appendix B, the $P(\mathbf{k})$ term can be rewritten as follows:

$$P(\mathbf{k})\sim \underbrace{C_p\frac{\partial}{\partial z}(\overline{\rho}\,\overline{\theta}\{w\}\cdot\{\pi'\})}_{\text{Divergence of vertical energy fluxes}} + \underbrace{C_p\overline{\rho}\,\overline{\theta}\{w\}\cdot\left\{\frac{\partial\pi'}{\partial z}\right\}}_{B(\mathbf{k})}, \tag{9}$$

where $B(\mathbf{k})$ is the buoyancy flux, which reflects the conversion between potential and kinetic energy. Combining the two flux terms in Eqs. (8) and (9), Eq. (5) becomes

$$\frac{\partial E(\mathbf{k})}{\partial t} = T(\mathbf{k}) + B(\mathbf{k}) + \mathrm{Flux}(\mathbf{k}) + D(\mathbf{k}). \tag{10}$$

Figure 8 shows the contribution of all the terms in Eqs. (5) and (10) as a function of horizontal wavenumber k_h summed over each wavenumber band. The dissipation term (Fig. 8c) has a negative contribution and mainly acts at small scales, as expected. When integrated over all the vertical levels, the flux term should go to zero; our calculation shows very small negatives (Fig. 8f). The reason is that the calculation is done over the levels below 15 km, and there is still a very small portion of the energy propagating to higher levels (Fig. 4c). Nonetheless, this contribution is tiny. Given that the $A(\mathbf{k})$ term could be written as the sum of the $T(\mathbf{k})$ term and a flux term, as shown in Eq. (8), we found an almost identical shape between the $A(\mathbf{k})$ term and the $T(\mathbf{k})$ term when integrated over the whole domain (0–15 km; Figs. 8a,d). The same argument can be applied to the $P(\mathbf{k})$ term (Fig. 8b) and the $B(\mathbf{k})$ term (Fig. 8e). Moreover, the consistency between these terms also implies the anelastic approximation used to

decompose these terms is valid. Also note that some of the terms shown here and in the following figures have peaks in the not-well-resolved gray-shaded spectral bands where subgrid mixing can be important. Our experiment with a different diffusion scheme gives similar results, which makes us more confident in the present finding. Nonetheless, as mentioned earlier, results in this region of wavenumber space should be interpreted with caution.

The sum of $T(\mathbf{k})$ over the wavenumbers shown in Fig. 8d (wavelength $<$ 800 km) is greater than zero. Since the sum of $T(\mathbf{k})$ over all wavenumbers adds to zero, there must be a loss of energy from the mean flow [i.e., $T(0)$ is negative]. This loss was implied by the downgradient mixing process shown in Fig. 2b. If we check the 6-h average of the $T(\mathbf{k})$ term (black line), positive values of $T(\mathbf{k})$ are found mainly in small scales, whereas $T(\mathbf{k})$ is close to 0 at scales greater than 100 km. This result seems to indicate that the small-scale features could directly withdraw energy from the mean flow, not necessarily through a cascade effect[2] from the large scales.

Compared to the $T(\mathbf{k})$ term (Fig. 8d), a more important source for $E(\mathbf{k})$ is the buoyancy production $B(\mathbf{k})$ term (Fig. 8e, conversion from potential energy). For the whole domain, $B(\mathbf{k})$ is positive at almost all the scales, with a peak at the small convective scales and a plateau at larger scales. A closer look at the $B(\mathbf{k})$ term at different time periods tells us that this plateau is closely related to the convective organization. Initially (0–2 h), $B(\mathbf{k})$ has a secondary maximum at around 100 km, which is roughly the length of the warm bubble line we added in the initial condition. At later times (3–4 h), this secondary maximum shifts toward larger scales because of the elongation of the convective systems in the meridional direction. At the end of the simulation, only two strong supercell-like systems remain; thus, $B(\mathbf{k})$ is slightly smaller, and the location of the secondary maximum of $B(\mathbf{k})$ also shifts toward the scale of the supercells.

The $E(\mathbf{k})$ budget analysis for different levels is given in Fig. 9, averaged over 0–4, 6–10, and 12–15 km, respectively. Since the kinetic energy spectra at these levels generally follow a similar quasi $-5/3$ power law (Fig. 7), the tendency of the spectra averaged every 2 h at these different levels also follows a similar shape to that in Fig. 5b. The dissipation term $D(\mathbf{k})$ (not plotted) also maintains its shape in Fig. 8c for each height level. Attention here will be focused on the $T(\mathbf{k})$, $B(\mathbf{k})$, and Flux($\mathbf{k}$) terms where significant differences between the vertical levels are found.

Figure 9e shows that in the upper troposphere, the diabatic heating is the strongest, which is reflected in $B(\mathbf{k})$ reaching its largest amplitude with a peak at the small convective scales and a plateau at larger scales consistent with the domain-averaged profile in Fig. 8. However, the strong positive contribution of $B(\mathbf{k})$ is largely cancelled by the Flux($\mathbf{k}$) term at this level (Fig. 9f). From Fig. 4c, we know that there is an increasing upward vertical energy transport in the upper troposphere (thus a positive value for the divergence of the energy flux), which explains the negative contribution of the Flux($\mathbf{k}$) term; the energy withdrawn by the energy flux term at this level is deposited into both the lower troposphere and the lower stratosphere.

In the lower troposphere, the buoyancy production has a smaller effect (Fig. 9b). It is positive at scales larger than 50 km, likely because of the formation of the cold pools that contain organized downdrafts and negative potential temperature anomalies due to evaporative cooling. The negative $B(\mathbf{k})$ at small scales is linked to the lifting parcels that overcome the convective inhibition (CIN). The total contribution of the $B(\mathbf{k})$ term integrated over all wavenumbers is largely cancelled by these two processes and may be even slightly negative at some levels (Fig. 4c). The input energy flux by the Flux($\mathbf{k}$) term (Fig. 9c) is the primary contributor for the lower troposphere; it is positive at all but the smallest (convective) scales. Note here both $B(\mathbf{k})$ and Flux($\mathbf{k}$) have little or negative contribution at small/convective scales; in the meantime, we know $D(\mathbf{k})$ also has a strong negative contribution at small scales; hence, to generate a $-5/3$ spectrum, $T(\mathbf{k})$ must balance all the negative contribution at small scales and remove some extra forcing at larger scales, as is shown in Fig. 9a. The shape of $T(\mathbf{k})$ in the lower troposphere suggests a ''downscale cascade'' scenario; however, this downscale cascade is still considerably different from that of the classic three-dimensional turbulence theory since the forcing of $B(\mathbf{k})$ and Flux($\mathbf{k}$) acts at all the scales, and unlike the classical turbulence theory, there is not a well-defined inertial subrange here. As also suggested by Waite and Snyder (2009), it is possible that the mesoscale kinetic energy spectrum does not arise from a cascade process.

Figure 9i shows that, in the lower stratosphere, convection-generated gravity waves inject a significant amount of energy mainly into small scales through the Flux($\mathbf{k}$) term. This term serves as the dominant source

[2] In classical turbulence theory, an energy cascade often refers to the transfer of energy from larger scales of motion to smaller scales, also called a direct energy cascade. If $T(\mathbf{k})$ is negative at relative larger scales and positive at small scales, then this is consistent with the cascade picture. Otherwise, it is not.

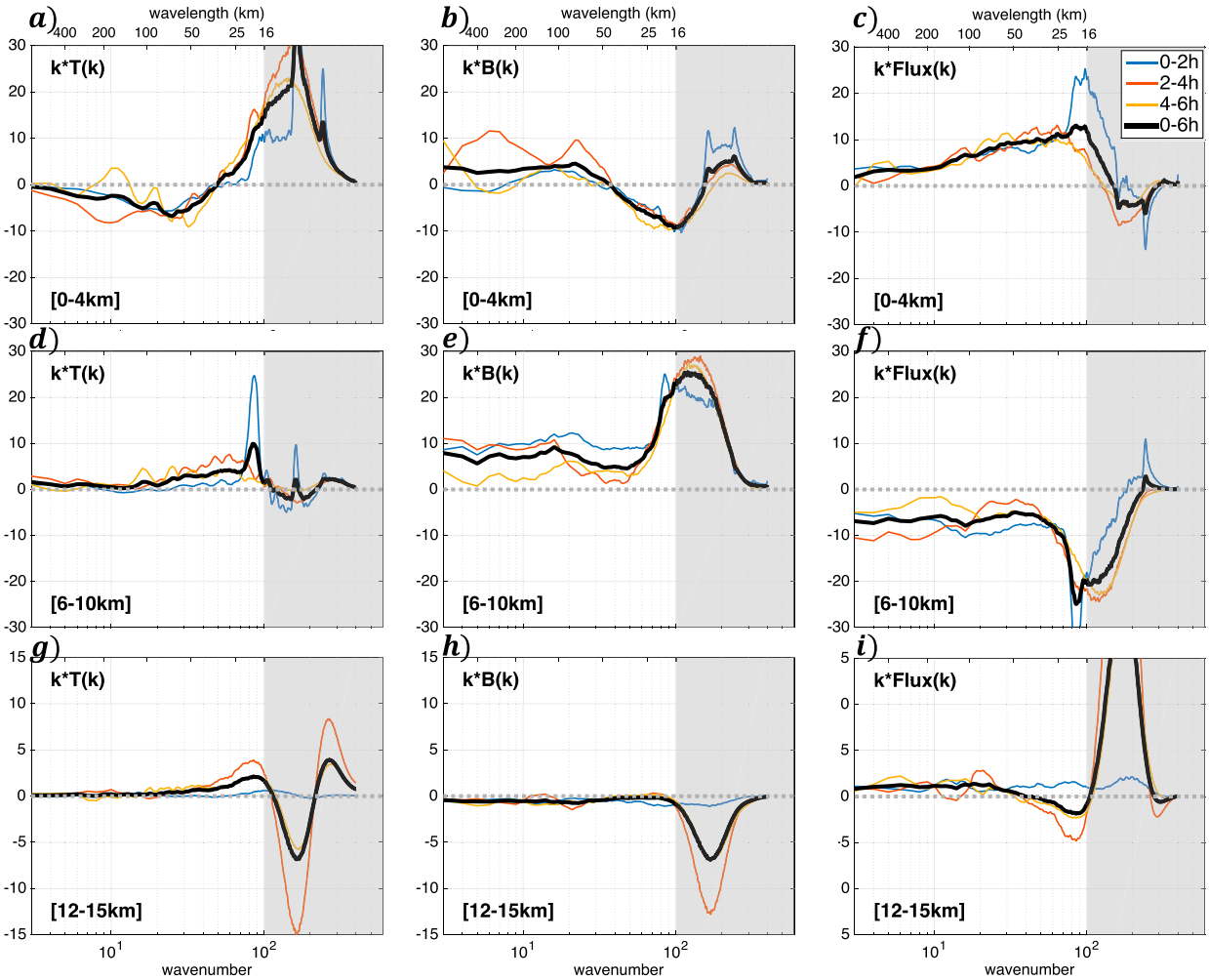

FIG. 9. Kinetic energy spectrum budget ($10^{-6}\,m^2\,s^{-3}\,kg\,m^{-3}$) analysis as in Fig. 8, but at different height levels: (a)–(c) the lower troposphere (0–4 km), (d)–(f) the upper troposphere (6–10 km), and (g)–(i) the lower stratosphere (12–15 km).

for the kinetic energy in this region. The $B(\mathbf{k})$ term has zero contribution everywhere except for the small convective scales, where it is slightly negative, likely because of some overshooting air parcels. The $T(\mathbf{k})$ term (Fig. 9g) acts to redistribute the injected energy into different scales to maintain the approximate $-5/3$ spectrum. Since the injected energy is mostly at small scales, we can find negative contribution of the $T(\mathbf{k})$ term at small scales and slight positive contribution of the $T(\mathbf{k})$ term at relative large scales (16–100 km).

In summary, although all the levels yield spectrum slopes of approximately $-5/3$, the underlying physical processes behind them are substantially different. Both the downscale process [e.g., $T(\mathbf{k})$ at the lower troposphere] and the upscale process [e.g., $T(\mathbf{k})$ at the lower stratosphere] appear to exist at the same time. The vertical energy flux terms are also critical for each specific level, implying a strong connection between the energy spectrum slopes at different vertical levels.

d. *Sensitivity experiments*

In the above simulations, we use an ensemble of 20 members to reduce the case dependency of our results. Yet all these members use the same model setup and physics schemes. To ensure that our results are robust, various sensitivity runs are also conducted. Figure 10 shows the kinetic energy spectrum for the DOUBLE experiment, where the horizontal size of the domain is doubled to 1600 km × 1600 km. A similar approximate $-5/3$ spectrum shows up again for this experiment. Moreover, additional experiments containing different model setups (e.g., different boundary conditions, reduced vertical layers, or different shear profiles) all give similar $-5/3$ spectra (not shown), implying that the $-5/3$

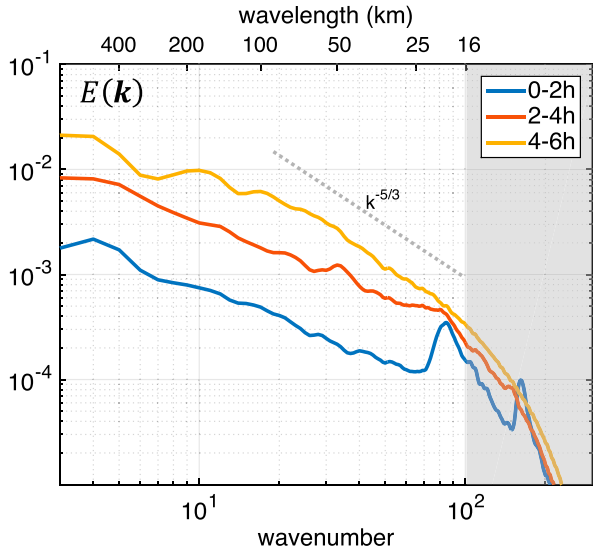

FIG. 10. Kinetic energy spectra ($m^2\,s^{-2}\,kg\,m^{-3}$) as in Fig. 5a, but for an experiment with the domain size doubled.

spectrum generated by the convective systems is not sensitive to the model setup.

The stratified turbulence theory proposed by Lindborg (2006) requires that vertical scales of U/N (U is the horizontal wind, while N is the Brunt–Väisälä frequency; U/N is around 1 km in the troposphere) be well resolved to drive the $-5/3$ mesoscale energy spectrum. In our simulation with only 40 vertical layers (a vertical grid spacing of ~500 m), the quasi $-5/3$ spectrum is still very clear. As we mentioned above, with the strong $B(\mathbf{k})$/Flux($\mathbf{k}$) terms at all scales, it is likely that the turbulent motion due to convective systems is different from what a classic turbulent theory would expect. The vertical resolution requirement for resolving the stratified turbulence proposed by Lindborg (2006) is not satisfied in our simulation. Note here that this does not mean that theories invoking stratified turbulence to explain the mesoscale spectrum and transition are invalid (Skamarock et al. 2014).

As for the impact of different model physics, microphysics is the only parameterization scheme used here, and we do not expect significant differences for the kinetic energy spectrum if other microphysics schemes were adopted. Hence, instead of changing any of the physics schemes, a constant Coriolis parameter ($f = 1.0 \times 10^{-4}\,s^{-1}$) is added to the model, which would affect the organization of the convective cells (Skamarock et al. 1994). Consistent with Skamarock et al. (1994), the evolution of the convective cells with the Coriolis effect exhibits significant asymmetries. At later hours of the simulation, the convective cells at the southern part of the domain center become much stronger than that in the control no-Coriolis simulations, while convective cells in the northern part decay. This asymmetry leads to a systematic reorientation, and the convective system moves toward the right of the wind shear. Because of this asymmetry, the convective cells, especially at the southern flank, tend to be more organized and form a quasi-squall-line structure. The intensity of the system is also stronger than that of the no-Coriolis experiment.

Figure 11 shows the kinetic energy spectrum for the experiment with the Coriolis effect. Compared with the no-Coriolis experiment, the energy spectrum is stronger, especially for the later times of the simulation, when the $-5/3$ spectrum extends to a scale of 400 km at the upper troposphere. The $E(\mathbf{k})$ budget analysis better explains the difference (Fig. 12). The results in the first 4 h (blue lines) are qualitatively and even quantitatively similar to the no-Coriolis experiment. After 4 h (red and yellow lines), because of the formation of the squall line on the southern flank, the buoyancy production $B(\mathbf{k})$ term becomes much stronger in the upper troposphere (Fig. 12e), which also causes the enhancement of the Flux($\mathbf{k}$) term (Fig. 12f) and adjustment of the $T(\mathbf{k})$ term (Fig. 12d). The $T(\mathbf{k})$ term shows some negatives at relatively smaller scales and is positive at larger scales in the upper troposphere (Fig. 12d), which implies some kind of upscale propagation of the kinetic energy. In the lower troposphere, the stronger convective systems with Coriolis effects also bring a peak of the $B(\mathbf{k})$ term at a scale of around 50 km (Fig. 12b), which leads to a negative $T(\mathbf{k})$ contribution at this scale (Fig. 12a). Significant differences with the no-Coriolis experiment also exist in the lower stratosphere, where stronger gravity waves generated by enhanced convection give a much stronger Flux($\mathbf{k}$) term (Fig. 12i) at small scales, leading to an enhanced upscale propagation by the $T(\mathbf{k})$ term (Fig. 12g). The positive contribution of the $T(\mathbf{k})$ term at relatively large scales (25–200-km wavelengths) is much more evident in this layer compared to the no-Coriolis experiment.

4. Discussion and concluding remarks

Using an ensemble of high-resolution cloud-model simulations, this study explores the kinetic energy spectrum of organized convective systems under vertical wind shear. Our results further confirm a recent finding by Durran and Weyn (2016) showing that convective systems alone could generate a background mesoscale kinetic energy spectrum with a slope proportional to the $-5/3$ power of the wavenumber. Building upon this result, the present study gives a picture of the growth

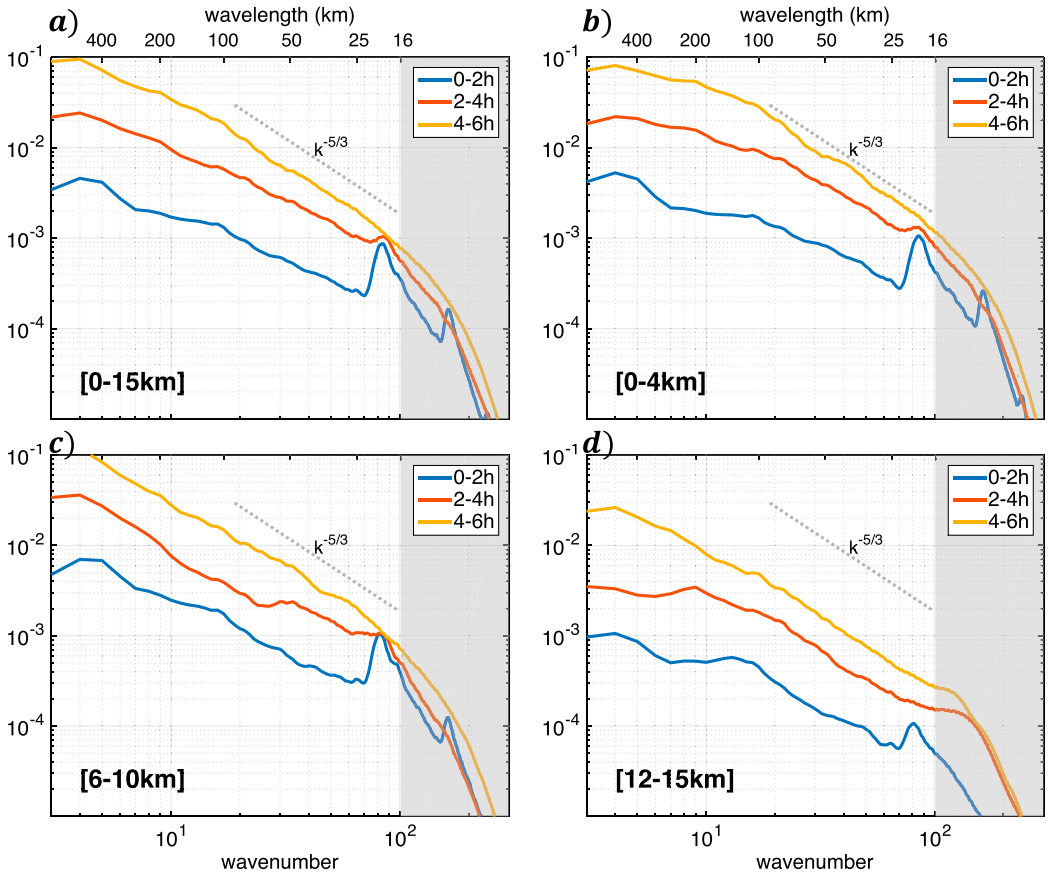

FIG. 11. Kinetic energy spectra ($m^2\,s^{-2}\,kg\,m^{-3}$) as in Figs. 5a and 7, but for an experiment with a constant Coriolis parameter added to the model ($f = 10^{-4}\,s^{-1}$).

processes of the −5/3 spectrum in this physical situation. At each specific height level, the physical processes actively contributing to the formation of the kinetic energy spectrum are as follows: 1) conversion from available potential energy to kinetic energy [buoyancy production or the $B(\mathbf{k})$ term], which primarily lies in the mid- to upper troposphere, with a peak at small convective scales and a plateau at larger scales; 2) divergence of the vertical energy flux [the Flux($\mathbf{k}$) term], which withdraws the energy generated by buoyancy in the upper troposphere and deposits it into both the lower stratosphere and the lower troposphere; and 3) filling out of the energy spectrum through nonlinear interactions [the $T(\mathbf{k})$ term] among different scales.

Sensitivity experiments of varying domain size or boundary conditions all give a similar approximate −5/3 spectrum in our simulations. Thus, our results are very robust in terms of different model settings. The −5/3 spectrum is also not affected by the organization of the convective systems. In the experiment with a constant nonzero Coriolis parameter, the interaction between different convective cells is greatly altered, especially at later times of the simulation. Thus, the forcing terms of the kinetic energy spectrum [e.g., the $B(\mathbf{k})$ term] also change accordingly. Yet the kinetic energy maintains the approximate −5/3 spectrum through adjustment of the nonlinear interaction [the $T(\mathbf{k})$ term].

Although the concept that deep convection is able to generate the −5/3 spectrum resembles Lilly's hypothesis, the building-up process of the spectrum is not the 2D inverse cascade as proposed by Lilly (1983). For each specific level, the divergence of vertical energy flux is critical, which means there are strong connections between different levels, and it is therefore a three-dimensional process. Moreover, buoyancy production and vertical flux of energy act at all the scales, so the dynamics cannot be described as an inertial-subrange cascade, as also pointed out by Waite and Snyder (2009). In addition, the filling out of the energy spectrum by nonlinear interactions varies greatly between different vertical levels. It goes through a downscale propagation in the lower troposphere to an upscale-like propagation

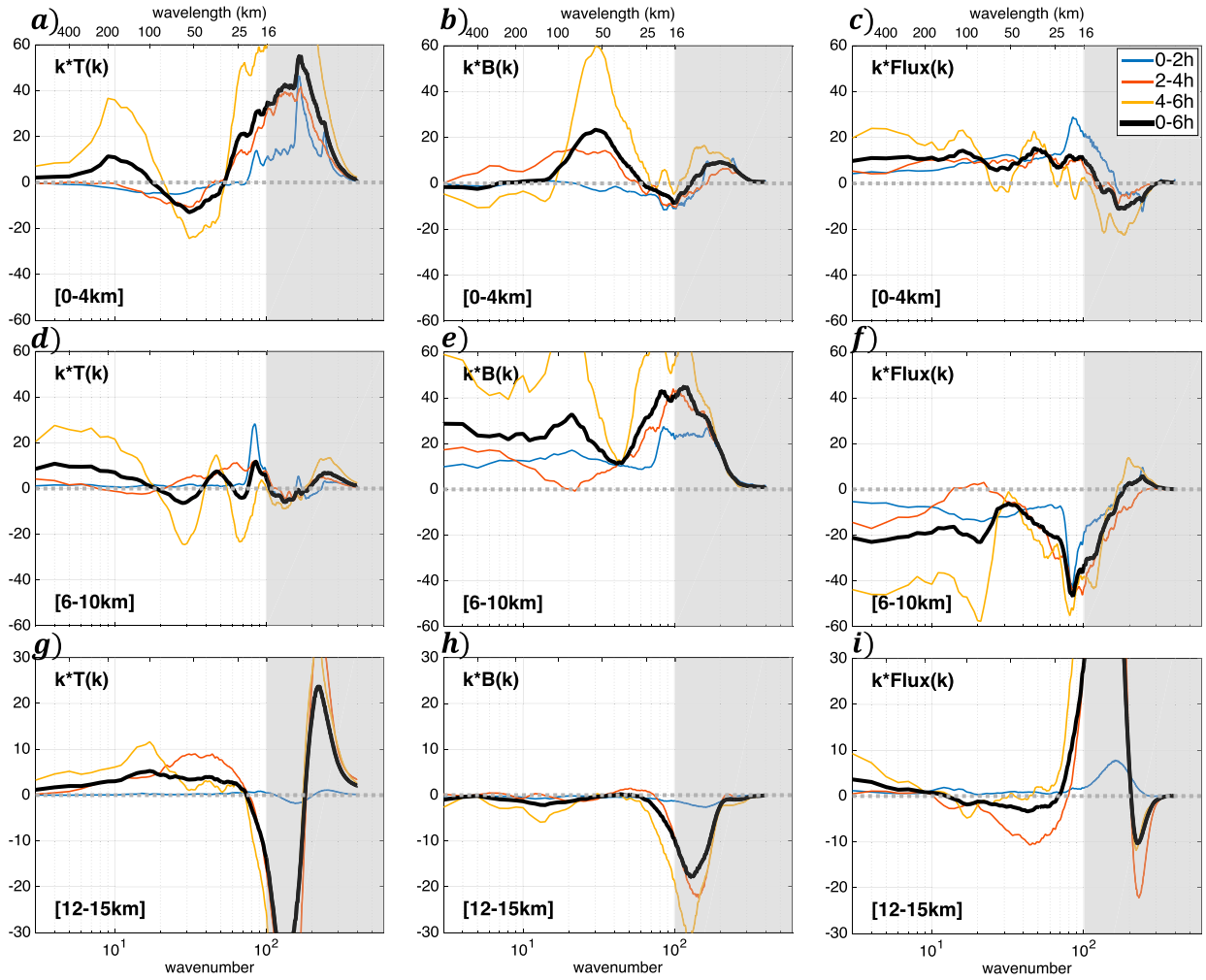

FIG. 12. As in Fig. 9, but for the experiment with a constant Coriolis parameter.

in the lower stratosphere. Both downscale and upscale processes happen at the same time but at different levels. We rarely find any true cascade signal in the simulations [consistent with Durran and Weyn (2016)]. Small-scale convection can even directly interact with the mean flow.

While convection is the ultimate source for the kinetic energy spectrum in our simulations, at high altitudes, where the aircraft observations lie, it is the convection-generated gravity waves that are the primary contributors to $E(\mathbf{k})$. Since moist convection is not the only source for the gravity waves, one can see why Waite and Snyder (2009) found a $-5/3$ spectrum in the lower troposphere of their dry simulation, since gravity waves are generated in association with a large-amplitude baroclinic wave. Nonetheless, moist convection is much more efficient and powerful in generating the gravity waves (Waite and Snyder 2013; Wei and Zhang 2014; Sun and Zhang 2016). Hence, a quasi-steady $-5/3$ spectrum could be built within hours after strong convection is initiated, as in our experiments. Recently, gravity wave–induced kinetic energy spectra have also been studied using superpressure balloon measurements (Podglajen et al. 2016). Being passively advected by winds in the lower stratosphere, these balloons provide direct and more accurate estimates of the kinetic energy spectra in the lower stratosphere. The slopes derived from this dataset are within the range of our simulation results, although their exact values vary from the equator to the poles.

A better understanding of the creation of the atmospheric energy spectrum is beneficial for the study of the atmospheric predictability. It has been proposed that the error growth behavior is closely related to the energy spectrum of the basic flow within which the errors grow (Lorenz 1969; Rotunno and Snyder 2008).

For a flow with energy spectra of power-law behavior k^{-p}, studies find that if the slope $p<3$, the error-doubling time decreases with scale, and the upscale spreading of initially small-scale error provides an effective limit to the predictability of such flows. This upscale error propagation scenario has been verified by numerous studies using full-physics models and simulations (e.g., Zhang et al. 2007; Selz and Craig 2015; Sun and Zhang 2016). However, if $p \geq 3$, it is concluded that there is no such limit. The implication of different physical processes behind the simulated $-5/3$ spectrum for the atmospheric predictability will be the subject of our future study.

We also want to emphasize that convection is not the only explanation for the observed $-5/3$ spectrum. We cannot rule out all the other hypotheses that have been proposed to explain the spectrum, although we have shown that some of them are not necessary in a moist environment. It is still an open question of how important convection is in the observed $-5/3$ spectrum of the real atmosphere. Moreover, although the current study clarifies the sources of $E(\mathbf{k})$ in these simulations of mesoscale convective systems, the authors have been unable to develop a simple explanation for why a $-5/3$ slope develops in the mesoscale range.

Acknowledgments. The authors thank Chris Snyder and Tiffany Shaw for thoughtful comments on the manuscript. Discussions with Dale Durran, Kerry Emanuel, Raf Ferrari, Joern Callies, and many other researchers on the subject were beneficial. Part of the research was conducted during the first author's summer visit to NCAR/MMM sponsored by the NCAR/Advanced Study Program Graduate Visitor Program. This research is partially supported by the National Science Foundation under AGS Grants 1114849 and 1305798. Computing was performed at the Texas Advanced Computing Center.

APPENDIX A

Discrete Cosine Transform

All the spectrum and budget analysis in this article is calculated using a discrete cosine transform (DCT) method defined as in Denis et al. (2002). A brief introduction of this method is given as follows.

For a two-dimensional field $f(i, j)$ of N_i by N_j grid points, the direct and inverse DCT are, respectively, defined as

$$\{f(m,n)\} = \beta(m)\beta(n)\sum_{i=0}^{i=N_i-1}\sum_{j=0}^{j=N_j-1} f(i,j) \times \cos\left[\frac{\pi m(i+1/2)}{N_i}\right]\cos\left[\frac{\pi n(j+1/2)}{N_j}\right], \tag{A1}$$

$$f(i,j) = \sum_{m=0}^{m=N_i-1}\sum_{n=0}^{n=N_j-1} \beta(m)\beta(n)\{f(m,n)\} \times \cos\left[\frac{\pi m(i+1/2)}{N_i}\right]\cos\left[\frac{\pi n(j+1/2)}{N_j}\right] \tag{A2}$$

with

$$\beta(m) = \begin{cases} \sqrt{\dfrac{1}{N_i}}, & m = 0 \\ \sqrt{\dfrac{2}{N_i}}, & m = 1,2,3,\ldots,N_i-1 \end{cases},$$

$$\beta(n) = \begin{cases} \sqrt{\dfrac{1}{N_j}}, & n = 0 \\ \sqrt{\dfrac{2}{N_j}}, & n = 1,2,3,\ldots,N_j-1 \end{cases}.$$

Let

$$\mathbf{e}_{m,n}(i,j) = \beta(m)\beta(n)\cos\left[\frac{\pi m(i+1/2)}{N_i}\right]\cos\left[\frac{\pi n(j+1/2)}{N_j}\right]; \tag{A3}$$

it can be proven that $\mathbf{e}_{m,n}(i, j)$ is a set of orthogonal basis, which satisfies

$$\sum_{i=0}^{i=N_i-1}\sum_{j=0}^{j=N_j-1} \mathbf{e}_{m_1,n_1}(i,j)\cdot\mathbf{e}_{m_2,n_2}(i,j) = \begin{cases} 1, & m_1 = m_2 \quad \text{and} \quad n_1 = n_2 \\ 0, & m_1 \neq m_2 \quad \text{or} \quad n_1 \neq n_2 \end{cases}. \tag{A4}$$

Utilizing Eqs. (A2) and (A4), we have,

$$\begin{aligned}
&\sum_{i=0}^{i=N_i-1}\sum_{j=0}^{j=N_j-1} f(i,j)\cdot g(i,j)\\
&=\sum_{i=0}^{i=N_i-1}\sum_{j=0}^{j=N_j-1}\left(\sum_{m=0}^{m=N_i-1}\sum_{n=0}^{n=N_j-1}\mathbf{e}_{m,n}(i,j)\{f(m,n)\}\right)\cdot\left(\sum_{m=0}^{m=N_i-1}\sum_{n=0}^{n=N_j-1}\mathbf{e}_{m,n}(i,j)\{g(m,n)\}\right)\\
&=\sum_{m=0}^{m=N_i-1}\sum_{n=0}^{n=N_j-1}\{f(m,n)\}\cdot\{g(m,n)\}\\
&=\sum_{\mathbf{k}}\{f(\mathbf{k})\}\cdot\{g(\mathbf{k})\}. \qquad \text{(A5)}
\end{aligned}$$

Assume $g(i, j) = f(i, j)$. Equation (A5) then implies that the total variance in the physical space equals the total variance in the spectral space. This serves as the foundation of Eq. (2) in the text. The energy spectrum can then be achieved by evaluating the variance of 2D fields as a function of different spatial scales. For a square domain, we associate each two-dimensional wavenumber pair $\mathbf{k}$ (m, n) with a single-scale parameter $k_h = (m^2 + n^2)^{1/2}$ so that each element (m, n) on a given circle with the origin $(m = 0, n = 0)$ has the same wavenumber. The one-dimensional wavenumber spectrum $E(k_h)$ is then obtained by taking the sum of the spectral variance over wavenumber bands $k_h - \Delta k/2 < k_h \le k_h + \Delta k/2$.

Also note here that the discrete cosine transform has no imaginary part; thus, the complex conjugate is not involved here, which is different from the discrete Fourier transform.

APPENDIX B

Decomposition of Advection and Pressure Term

The advection term is defined as,

$$\begin{aligned}
A(\mathbf{k}) &= -\overline{\rho}\{\mathbf{u}\}\cdot\left\{\mathbf{u}\cdot\nabla_h\mathbf{u}+w\frac{\partial\mathbf{u}}{\partial z}\right\}\\
&= -\overline{\rho}\{\mathbf{u}\}\cdot\left\{\left(\mathbf{u}\cdot\nabla_h\mathbf{u}+\frac{\mathbf{u}(\nabla_h\cdot\mathbf{u})}{2}-\frac{\mathbf{u}(\nabla_h\cdot\mathbf{u})}{2}\right.\right.\\
&\quad\left.\left.+\frac{1}{2}\left[w\frac{\partial\mathbf{u}}{\partial z}+\frac{\partial(w\mathbf{u})}{\partial z}-\mathbf{u}\frac{\partial w}{\partial z}\right]\right)\right\}. \qquad \text{(B1)}
\end{aligned}$$

Rearranging all the terms in the bracket, we have

$$\begin{aligned}
A(\mathbf{k}) &= -\overline{\rho}\{\mathbf{u}\}\cdot\left\{\mathbf{u}\cdot\nabla_h\mathbf{u}+\frac{\mathbf{u}(\nabla_h\cdot\mathbf{u})}{2}\right\}-\frac{1}{2}\overline{\rho}\{\mathbf{u}\}\cdot\left\{w\frac{\partial\mathbf{u}}{\partial z}\right\}\\
&\quad+\frac{1}{2}\overline{\rho}\{\mathbf{u}\}\cdot\left\{\mathbf{u}(\nabla_h\cdot\mathbf{u})+\mathbf{u}\frac{\partial w}{\partial z}\right\}\\
&\quad-\frac{1}{2}\overline{\rho}\{\mathbf{u}\}\cdot\left\{\frac{\partial(w\mathbf{u})}{\partial z}\right\}\\
&= -\overline{\rho}\{\mathbf{u}\}\cdot\left\{\mathbf{u}\cdot\nabla_h\mathbf{u}+\frac{\mathbf{u}(\nabla_h\cdot\mathbf{u})}{2}\right\}-\frac{1}{2}\overline{\rho}\{\mathbf{u}\}\cdot\left\{w\frac{\partial\mathbf{u}}{\partial z}\right\}\\
&\quad+\underline{\frac{1}{2}\overline{\rho}\{\mathbf{u}\}\cdot\left\{\mathbf{u}(\nabla_h\cdot\mathbf{u})+\mathbf{u}\frac{\partial w}{\partial z}\right\}}\\
&\quad-\frac{1}{2}\frac{\partial(\overline{\rho}\{\mathbf{u}\}\cdot\{w\mathbf{u}\})}{\partial z}+\frac{1}{2}\overline{\rho}\left\{\frac{\partial\mathbf{u}}{\partial z}\right\}\cdot\{w\mathbf{u}\}+\underline{\frac{1}{2}\frac{\partial\overline{\rho}}{\partial z}(\{\mathbf{u}\}\cdot\{w\mathbf{u}\})}\ . \qquad \text{(B2)}
\end{aligned}$$

Notice here $\partial\overline{\rho}/\partial z$ and $\overline{\rho}$ are both constant at each height level. Utilizing the continuity equation under anelastic approximation,

$$(\nabla_h\cdot\mathbf{u})+\frac{\partial w}{\partial z}+\frac{w}{\overline{\rho}}\frac{\partial\overline{\rho}}{\partial z}=0, \qquad \text{(B3)}$$

and substituting Eq. (B3) for the underlined terms in Eq. (B2), we can find that the sum of the two underlined terms in Eq. (B2) goes to zero. Thus, we have

$$A(\mathbf{k}) = \underbrace{-\overline{\rho}\{\mathbf{u}\}\cdot\left\{\mathbf{u}\cdot\nabla_h\mathbf{u}+\frac{\mathbf{u}(\nabla_h\cdot\mathbf{u})}{2}\right\}-\frac{1}{2}\overline{\rho}\{\mathbf{u}\}\cdot\left\{w\frac{\partial\mathbf{u}}{\partial z}\right\}+\frac{1}{2}\overline{\rho}\left\{\frac{\partial\mathbf{u}}{\partial z}\right\}\cdot\{w\mathbf{u}\}}_{T(\mathbf{k})}$$
$$\underbrace{-\frac{1}{2}\frac{\partial(\overline{\rho}\{\mathbf{u}\}\cdot\{w\mathbf{u}\})}{\partial z}}_{\text{Divergence of vertical energy flux}}. \tag{B4}$$

Under the double periodic boundary condition, the sum of the $T(\mathbf{k})$ term in Eq. (B4) over all the wavenumbers is zero. The proof is as follows. According to Eq. (A5),

$$\begin{aligned}\sum_{\mathbf{k}} T(\mathbf{k}) &= \sum_{\mathbf{k}}\left[-\overline{\rho}\{\mathbf{u}\}\cdot\left\{\mathbf{u}\cdot\nabla_h\mathbf{u}+\frac{\mathbf{u}(\nabla_h\cdot\mathbf{u})}{2}\right\}-\frac{1}{2}\overline{\rho}\{\mathbf{u}\}\cdot\left\{w\frac{\partial\mathbf{u}}{\partial z}\right\}+\frac{1}{2}\overline{\rho}\left\{\frac{\partial\mathbf{u}}{\partial z}\right\}\cdot\{w\mathbf{u}\}\right]\\ &= -\overline{\rho}\sum_{i,j}\left(\mathbf{u}\cdot\left[\mathbf{u}\cdot\nabla_h\mathbf{u}+\frac{\mathbf{u}(\nabla_h\cdot\mathbf{u})}{2}\right]\right)-\frac{1}{2}\overline{\rho}\sum_{i,j}\left[\mathbf{u}\cdot\left(w\frac{\partial\mathbf{u}}{\partial z}\right)-\frac{\partial\mathbf{u}}{\partial z}\cdot(w\mathbf{u})\right]\\ &= -\overline{\rho}\sum_{i,j}\left(\mathbf{u}\cdot\left[\mathbf{u}\cdot\nabla_h\mathbf{u}+\frac{\mathbf{u}(\nabla_h\cdot\mathbf{u})}{2}\right]\right)\\ &= -\frac{\overline{\rho}}{L^2}\int_s\nabla\cdot\left[\frac{1}{2}\mathbf{u}(\mathbf{u}\cdot\mathbf{u})\right]ds = -\frac{\overline{\rho}}{L^2}\int_l\frac{1}{2}\mathbf{u}(\mathbf{u}\cdot\mathbf{u})\mathbf{u}\cdot\mathbf{n}\,dl,\end{aligned} \tag{B5}$$

where s represents the horizontal domain, l represents the lateral boundaries of s, and $\mathbf{n}$ denotes the unit vector pointing along the outward normal to l. A double periodic lateral boundary condition gives a zero result to the integration along the boundary.

For the pressure term, it is easier to prove the decomposition in Eq. (9) under the Fourier transform framework. Under Fourier transformation, the pressure term is written as follows:

$$P(\mathbf{k}) = -\overline{\rho}\tilde{u}^*\cdot\mathcal{F}(C_p\theta_v\nabla_h\pi'),\text{ c.c.},$$

where $\tilde{u}$ and $\mathcal{F}(\mathbf{u})$ represent the spectral coefficients of Fourier transform, and an asterisk or c.c. denotes the complex conjugate. The decomposition of the pressure term is shown here:

$$\begin{aligned}P(\mathbf{k}) &= -\overline{\rho}\tilde{\mathbf{u}}^*\cdot\mathcal{F}(C_p\theta_v\nabla_h\pi')+\text{c.c.}\\ &\sim -\overline{\rho}C_p\overline{\theta}\tilde{\mathbf{u}}^*\cdot\mathcal{F}(\nabla_h\pi')+\text{c.c.}\\ &= -\overline{\rho}C_p\overline{\theta}\tilde{\mathbf{u}}^*\cdot\mathcal{F}(i\mathbf{k}\pi')+\text{c.c.}\\ &= \overline{\rho}C_p\overline{\theta}(\tilde{\mathbf{u}}\cdot i\mathbf{k})^*\tilde{\pi}'+\text{c.c.}\\ &= \overline{\rho}C_p\overline{\theta}[\mathcal{F}(\nabla_h\cdot\mathbf{u})]^*\tilde{\pi}'+\text{c.c.}\end{aligned} \tag{B6}$$

Using the improved anelastic approximation [simply using Eq. (B3) will give similar results; we use this improved anelastic approximation to be as accurate as we can], Eq. (7) of Durran (1989),

$$\nabla_h\cdot\mathbf{u}+\frac{1}{\overline{\rho}\,\overline{\theta}}\frac{\partial}{\partial z}(\overline{\rho}\,\overline{\theta}w) = \frac{H}{C_p\overline{\rho}\,\overline{\theta}\,\overline{\pi}}, \tag{B7}$$

we have

$$\begin{aligned}P(\mathbf{k}) &\sim \overline{\rho}C_p\overline{\theta}\left[\frac{H}{C_p\overline{\rho}\,\overline{\theta}\,\overline{\pi}}-\frac{1}{\overline{\rho}\,\overline{\theta}}\frac{\partial}{\partial z}(\overline{\rho}\,\overline{\theta}w)\right]^*\tilde{\pi}'+\text{c.c.}\\ &= \frac{\tilde{H}^*\tilde{\pi}'}{\overline{\pi}}-C_p\frac{\partial}{\partial z}(\overline{\rho}\,\overline{\theta}\tilde{w}^*\tilde{\pi}')+C_p\overline{\rho}\,\overline{\theta}\tilde{w}^*\frac{\partial\tilde{\pi}'}{\partial z}+\text{c.c.}\\ &\sim \underbrace{C_p\frac{\partial}{\partial z}(\overline{\rho}\,\overline{\theta}\{w\}\cdot\{\pi'\})}_{\text{Divergence of vertical energy fluxes}}+\underbrace{C_p\overline{\rho}\,\overline{\theta}\{w\}\cdot\left\{\frac{\partial\pi'}{\partial z}\right\}}_{B(\mathbf{k})}.\end{aligned} \tag{B8}$$

When using the discrete cosine transform method, the complex conjugate will disappear. We also neglect the direct diabatic heating term when showing the results since it is several orders of magnitude smaller than the other two terms.

REFERENCES

Bierdel, L., C. Snyder, S.-H. Park, and W. C. Skamarock, 2016: Accuracy of rotational and divergent kinetic energy spectra diagnosed from flight-track winds. *J. Atmos. Sci.*, **73**, 3273–3286, doi:10.1175/JAS-D-16-0040.1.

Callies, J., R. Ferrari, and O. Buhler, 2014: Transition from geostrophic turbulence to inertia–gravity waves in the atmospheric energy spectrum. *Proc. Natl. Acad. Sci. USA*, **111**, 17 033–17 038, doi:10.1073/pnas.1410772111.

Charney, J. G., 1971: Geostrophic turbulence. *J. Atmos. Sci.*, **28**, 1087–1095, doi:10.1175/1520-0469(1971)028<1087:GT>2.0.CO;2.

Cho, J. Y. N., R. E. Newell, and J. D. Barrick, 1999: Horizontal wavenumber spectra of winds, temperature, and trace gases during the Pacific Exploratory Missions: 2. Gravity waves, quasi-two-dimensional turbulence, and vortical modes. *J. Geophys. Res.*, **104**, 16 297–16 308, doi:10.1029/1999JD900068.

Davis, C. A., and M. L. Weisman, 1994: Balanced dynamics of mesoscale vortices produced in simulated convective systems. *J. Atmos. Sci.*, **51**, 2005–2030, doi:10.1175/1520-0469(1994)051<2005:BDOMVP>2.0.CO;2.

Denis, B., J. Côté, and R. Laprise, 2002: Spectral decomposition of two-dimensional atmospheric fields on limited-area domains using the discrete cosine transform (DCT). *Mon. Wea. Rev.*, **130**, 1812–1829, doi:10.1175/1520-0493(2002)130<1812:SDOTDA>2.0.CO;2.

Durran, D. R., 1989: Improving the anelastic approximation. *J. Atmos. Sci.*, **46**, 1453–1461, doi:10.1175/1520-0469(1989)046<1453:ITAA>2.0.CO;2.

——, and J. A. Weyn, 2016: Thunderstorms don't get butterflies. *Bull. Amer. Meteor. Soc.*, **97**, 237–243, doi:10.1175/BAMS-D-15-00070.1.

Hamilton, K., Y. O. Takahashi, and W. Ohfuchi, 2008: The mesoscale spectrum of atmospheric motions investigated in a very fine resolution global general circulation model. *J. Geophys. Res.*, **113**, D18110, doi:10.1029/2008JD009785.

Klemp, J. B., J. Dudhia, and A. D. Hassiotis, 2008: An upper gravity-wave absorbing layer for NWP applications. *Mon. Wea. Rev.*, **136**, 3987–4004, doi:10.1175/2008MWR2596.1.

Koshyk, J. N., K. Hamilton, and J. D. Mahlman, 1999: Simulation of $k^{-5/3}$ mesoscale spectral regime in the GFDL SKYHI general circulation model. *Geophys. Res. Lett.*, **26**, 843–846, doi:10.1029/1999GL900128.

Lilly, D. K., 1983: Stratified turbulence and the mesoscale variability of the atmosphere. *J. Atmos. Sci.*, **40**, 749–761, doi:10.1175/1520-0469(1983)040<0749:STATMV>2.0.CO;2.

Lindborg, E., 2006: The energy cascade in a strongly stratified fluid. *J. Fluid Mech.*, **550**, 207–242, doi:10.1017/S0022112005008128.

——, 2015: A Helmholtz decomposition of structure functions and spectra calculated from aircraft data. *J. Fluid Mech.*, **762**, R4, doi:10.1017/jfm.2014.685.

Lorenz, E. N., 1969: Atmospheric predictability as revealed by naturally occurring analogues. *J. Atmos. Sci.*, **26**, 636–646, doi:10.1175/1520-0469(1969)26<636:APARBN>2.0.CO;2.

Morrison, H., G. Thompson, and V. Tatarskii, 2009: Impact of cloud microphysics on the development of trailing stratiform precipitation in a simulated squall line: Comparison of one- and two-moment schemes. *Mon. Wea. Rev.*, **137**, 991–1007, doi:10.1175/2008MWR2556.1.

Nastrom, G. D., and K. S. Gage, 1985: A climatology of atmospheric wavenumber spectra observed by commercial aircraft. *J. Atmos. Sci.*, **42**, 950–960, doi:10.1175/1520-0469(1985)042<0950:ACOAWS>2.0.CO;2.

Peng, J., L. Zhang, Y. Luo, and Y. Zhang, 2014: Mesoscale energy spectra of the mei-yu front system. Part I: Kinetic energy spectra. *J. Atmos. Sci.*, **71**, 37–55, doi:10.1175/JAS-D-13-085.1.

Podglajen, A., A. Hertzog, R. Plougonven, and B. Legras, 2016: Lagrangian temperature and vertical velocity fluctuations due to gravity waves in the lower stratosphere. *Geophys. Res. Lett.*, **43**, 3543–3553, doi:10.1002/2016GL068148.

Rotunno, R., and C. Snyder, 2008: A generalization of Lorenz's model for the predictability of flows with many scales of motion. *J. Atmos. Sci.*, **65**, 1063–1076, doi:10.1175/2007JAS2449.1.

Selz, T., and G. C. Craig, 2015: Upscale error growth in a high-resolution simulation of a summertime weather event over Europe. *Mon. Wea. Rev.*, **143**, 813–827, doi:10.1175/MWR-D-14-00140.1.

Skamarock, W. C., 2004: Evaluating mesoscale NWP models using kinetic energy spectra. *Mon. Wea. Rev.*, **132**, 3019–3032, doi:10.1175/MWR2830.1.

——, M. L. Weisman, and J. B. Klemp, 1994: Three-dimensional evolution of simulated long-lived squall lines. *J. Atmos. Sci.*, **51**, 2563–2584, doi:10.1175/1520-0469(1994)051<2563:TDEOSL>2.0.CO;2.

——, and Coauthors, 2008: A description of the Advanced Research WRF version 3. NCAR Tech. Note NCAR/TN-475+STR, 113 pp., doi:10.5065/D68S4MVH.

——, S.-H. Park, J. B. Klemp, and C. Snyder, 2014: Atmospheric kinetic energy spectra from global high-resolution nonhydrostatic simulations. *J. Atmos. Sci.*, **71**, 4369–4381, doi:10.1175/JAS-D-14-0114.1.

Sun, Y., and F. Zhang, 2016: Intrinsic versus practical limits of atmospheric predictability and the significance of the butterfly effect. *J. Atmos. Sci.*, **73**, 1419–1438, doi:10.1175/JAS-D-15-0142.1.

Tulloch, R., and K. S. Smith, 2006: A theory for the atmospheric energy spectrum: Depth-limited temperature anomalies at the tropopause. *Proc. Natl. Acad. Sci. USA*, **103**, 14 690–14 694, doi:10.1073/pnas.0605494103.

VanZandt, T. E., 1982: A universal spectrum of buoyancy waves in the atmosphere. *Geophys. Res. Lett.*, **9**, 575–578, doi:10.1029/GL009i005p00575.

Waite, M. L., and C. Snyder, 2009: The mesoscale kinetic energy spectrum of a baroclinic life cycle. *J. Atmos. Sci.*, **66**, 883–901, doi:10.1175/2008JAS2829.1.

——, and ——, 2013: Mesoscale energy spectra of moist baroclinic waves. *J. Atmos. Sci.*, **70**, 1242–1256, doi:10.1175/JAS-D-11-0347.1.

Wei, J., and F. Zhang, 2014: Mesoscale gravity waves in moist baroclinic jet–front systems. *J. Atmos. Sci.*, **71**, 929–952, doi:10.1175/JAS-D-13-0171.1.

——, and ——, 2015: Tracking gravity waves in moist baroclinic waves. *J. Adv. Model. Earth Syst.*, **7**, 67–91, doi:10.1002/2014MS000395.

——, ——, and J. H. Richter, 2016: An analysis of gravity wave spectral characteristics in moist baroclinic jet–front systems. *J. Atmos. Sci.*, **73**, 3133–3155, doi:10.1175/JAS-D-15-0316.1.

Weisman, M. L., and J. B. Klemp, 1982: The dependence of numerically simulated convective storms on vertical wind shear and buoyancy. *Mon. Wea. Rev.*, **110**, 504–520, doi:10.1175/1520-0493(1982)110<0504:TDONSC>2.0.CO;2.

Zhang, F., N. Bei, R. Rotunno, C. Snyder, and C. C. Epifanio, 2007: Mesoscale predictability of moist baroclinic waves: Convection-permitting experiments and multistage error growth dynamics. *J. Atmos. Sci.*, **64**, 3579–3594, doi:10.1175/JAS4028.1.